Journal of Applied Sciences and Nanotechnology

Journal homepage: jasn.uotechnology.edu.iq

Synthesis and Characterization of TiO_2 Nanoparticles via Hydrothermal and Sol-Gel Technique for Water Treatment

[1]Aya Talal Sami*, [1]Selma M. H. Al-Jawad, [2]Natheer Jamal Imran

[1]College of Applied Sciences, University of Technology-Iraq, Iraq
[2]Research and Technology Center of Environment, Water and Renewable Energy, Scientific Research Commission, Ministry of Higher Education and Scientific Research, Iraq

ARTICLE INFO

Article history:
Received: November, 02, 2024
Accepted: June, 09, 2025
Available online: September, 10, 2025

Keywords:
TiO_2 nanoparticles,
Hydrothermal,
Sol-gel,
Photocatalytic activity,
Wastewater

Corresponding Author:
Aya Talal Sami
as.18.44@grad.uotechnology.edu.iq

ABSTRACT

Titanium dioxide (TiO_2) has attracted significant interest for water treatment applications due to its non-toxic nature and high photocatalytic activity. In this study, TiO_2 nanoparticles were synthesized using two different methods to evaluate their photocatalytic performance in degrading organic contaminants from wastewater. Sample S1 was prepared via the sol–gel method, while sample S2 was synthesized using a hydrothermal approach. X-ray diffraction (XRD) analysis confirmed that both samples crystallized in the tetragonal anatase phase, with average crystallite sizes of 12 nm for S1 and 29 nm for S2. Field-emission scanning electron microscopy (FE-SEM) revealed spherical particles with uniform morphology for both samples. Optical absorbance measurements conducted using UV–vis spectrophotometry yielded estimated band gap energies of 3.2 eV for S1 and 3.0 eV for S2. Both samples demonstrated notable photocatalytic activity; however, S2 exhibited superior degradation efficiency against organic pollutants, indicating that the hydrothermally synthesized TiO_2 possesses enhanced photocatalytic properties. These results underscore the potential of TiO_2 particularly that synthesized via hydrothermal methods, as an effective photocatalyst for wastewater treatment applications.

https://doi.org/10.53293/jasn.2025.7539.1328, Department of Applied Sciences, University of Technology - Iraq.

Introduction

Conventional wastewater treatment techniques can no longer adequately filter highly contaminated water. Numerous methods have lately been studied and shown to be effective, including reverse osmosis, flocculation, activated sludge, electrochemical oxidation, and adsorption using activated carbon [1]. One major drawback of these approaches is that they produce a more concentrated phase with contaminants. However, recent developments have been in the oxidative decay of organic molecules dispersed or dissolved in water. Among the various advanced oxidation methodologies, heterogeneous photocatalysis has been recognized as a potentially effective destructive technique that can help most organic contaminants mineralize completely [2]. AOPs, or advanced oxidation processes, are very efficient for treating toxic wastewater and non-biodegradable organic pollutants. Certain chemical reactions in aqueous solutions produce strong reactive species in AOPs, such as

hydroxyl radicals (•OH). Hydroxyl radicals can break down even the most resilient organic compounds, converting them into organic compounds and byproducts like CO_2 and H_2O that are comparatively less persistent [3]. Nanostructured materials have attracted a lot of interest from scientists in a variety of environmental fields because of their exceptional qualities, high specific surface area, surface and dimensional phenomena, low density, unique optical properties, increased permeability, and a wide range of potential uses [4]. Titanium dioxide nanoparticles (TiO_2 NPs) are widely used in environmental remediation efforts to aid in the breakdown of pollutants found in aqueous environments because of their exceptional physicochemical properties [5]. Titanium dioxide is categorized as an n-type semiconductor because the amount of oxygen loss in the lattice increases its conductivity. Additionally, it has high photocatalytic activity and excellent transparency in the visible region, which are influenced by the crystal structure, surface morphology, and crystallization of the involved TiO_2 photocatalyst, as well as chemical stability, a high dielectric constant, a high refractive index, and nontoxicity. It is also inexpensive, easy to synthesize, has a wide band gap, is highly photostable [6], and is stable in a variety of environments [7]. In nature, anatase, rutile, and brookite are the three distinct crystalline phases of titanium dioxide (TiO_2) [8]. Due to its remarkable photocatalytic activity, anatase TiO_2 has become one of the most widely recognized photocatalysts after several decades of development [9]. The photocatalytic activity of TiO_2 relies on the generation of electron/hole (e-/h+) pairs when exposed to light, which triggers chemical reactions by producing radical species on the surface of TiO_2 [10]. Titanium dioxide nanoparticles can be prepared using a variety of methods, including the sol-gel method, chemical vapor deposition, hydrothermal method, and microemulsion [11]. The hydrothermal method has proved to be a relatively simple technique due to its lower cost and simple experimental conditions [12]. Unlike other chemical processes, this method produces nanoscale particles with unique physical properties. Like hydrothermal synthesis, the sol-gel method has the advantage of operating at lower pressure and temperature. This technique provides the flexibility to alter the nanoparticles' composition and microstructural characteristics, depending on the chemistry of the precursor and the particular synthesis parameters used [13]. In our previous work, we studied the preparation of TiO_2 using the hydrothermal method for photocatalytic activity [14]. The results from our previous work were used in comparison with the sol-gel method. This paper described the synthesis and characterization of TiO_2 nanoparticles made using hydrothermal and sol-gel techniques. The prepared samples were characterized using Fourier transform infrared spectroscopy, UV-visible spectrophotometer, zeta potential, X-ray diffraction, and field emission scanning electron microscopy (FE-SEM). The photocatalytic performance of TiO_2 was investigated by the degradation of wastewater's organic contaminants.

2. Experimental Procedure

2.1 Materials

Titanium tetra isopropoxide (TTIP) [Ti ($OCH(CH_3)_4$], 98%; Merck] from Sigma-Aldrich, Sodium hydroxide [NaOH, 98%; Merck], as well as ethanol with a purity of (99.99%) and deionized water. No additional purification was done before using any of the reagents.

2.2 Preparation of TiO_2 NPs

We have created titanium dioxide nanoparticles using both the sol-gel and hydrothermal processes to perform comparative analysis. To achieve complete dissolution, 50 mL of deionized water (DIW) and 2.5 mL of TTIP are combined and swirled for three hours in the hydrothermal process. The mixture was stirred for half an hour after 0.1 mL of NaOH was added dropwise. The pH level was meticulously regulated at 7. Thereafter, the resulting combination was transferred into a Teflon-lined stainless-steel autoclave and exposed to a temperature of 180 °C for 24 hours. The precipitate obtained was rigorously washed via centrifugation with distilled water and ethanol and, thereafter, subjected to a drying process conducted at 80 °C for three hours. The dried sample was then annealed for five hours at 400 °C and given the sample number "S1." For the sol-gel process, 150 mL of ethanol and 10 mL of deionized water were combined and stirred continuously, and then 9 mL of TTIP was added while the mixture was kept at 70 °C with a paraffin oil bath. The solution was stirred continuously for 4 h. Following centrifugation and a water wash to remove any remaining contaminants, the solution was left in an oven set at 60 °C for three hours. The resulting TiO_2 powder was referred to as sample "S2" after being annealed for three hours at 400 °C.

2.3 Characterizations

By analyzing X-ray diffraction (model XRD-6000, Shimadzu, Japan) using Cu Kα radiation (1.5406 Å) in the range (20°–80°), the crystal structure of TiO_2 nanopowder was determined. A UV-visible spectrophotometer (UV-1800, Shimadzu) was used to obtain optical absorption spectra in the wavelength range of 200–1100 nm. A field emission scanning electron microscope (FE-SEM; ZEISS SIGMA VP) equipped with an energy-dispersive X-ray spectroscope (EDS) was used to analyze the final product's morphologies. The instrument ran with a 10 kV acceleration. The Sample's infrared spectra (Shimadzu IR Affinity) were recorded using an FT-IR spectrometer over the 400–4000 cm^{-1} range. Zeta potential measurements were determined using Zeta Plus (Brookhaven).

2.4 Photocatalytic Activity

The decay of organic contaminants in wastewater from petroleum refineries has been investigated using both S1 and S2 samples as photocatalysts. The Al-Dura refinery in Baghdad, Iraq, is where this PRWW was taken. The photocatalytic activity of S1 and S2 samples for the treatment of wastewater was studied using a closed experimental homemade setup. 1000 mL of wastewater from a petroleum refinery with (0.01 mg L^{-1}) of TiO_2 nanopowder was put into the tank for the initial photocatalytic experiment. A UV lamp (220 volts, 6-watt, 50 Hz) was used to irradiate the solution for up to 30 minutes for each specimen. The solution's pH was kept at 7. The solution was pumped from the tank to the UV light using a feeding suction pump. Following the standard procedures for wastewater analysis, the wastewater was described and examined for oil and grease, TOC, and COD. An infrared spectrophotometer (OCMA-350, Japan) was used to measure the amount of oil and grease in effluent. A Hach-3900 spectrophotometer was used to measure the chemical oxygen demand (COD) and total organic carbon (TOC) in a strong acid environment utilizing a solution of dichromate as the oxidant. The carrier gas used for analyses of gas chromatography (Shimadzu 2010, Japan) was helium (5 mL/min). For one minute, the column's temperature was kept at 40 °C. After that, it was raised to 120 °C at a rate of 25 °C per minute, 160 °C at a rate of 10 °C per minute, and finally to 300 °C at a rate of 5 °C per minute. It stayed at the highest temperature for fifteen minutes. The detector (FID) temperature was kept at 330 °C. Using Equation 1, the efficiency of photocatalytic decay of organic contaminants in wastewater from petroleum refineries was determined.

$$\text{Photocatalytic degradation rate (\%)} = \frac{C_i - C_f}{C_i} \times 100 \quad (1)$$

where the final concentration is denoted by C_f and the beginning concentration by C_i [15]. UV light TiO_2 photocatalysis mechanism can be summarized in **Fig. 1**.

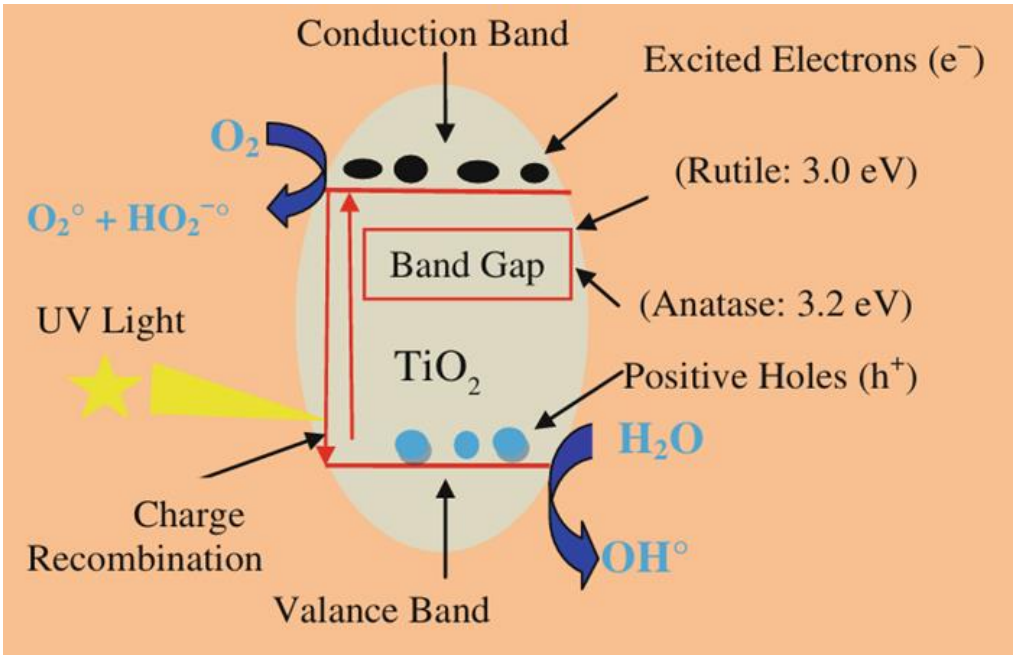

Figure 1: Mechanism of UV light-induced TiO_2 photocatalysis.

3. Results and Discussion

3.1 X-ray Diffraction Spectra

The synthesized powder specimens' crystalline structure and phase composition were investigated using X-ray diffraction (XRD) analyses. **Fig. 2** illustrates the X-ray diffraction (XRD) patterns of S1 and S2 samples obtained within the angular range of 10-90°. **Fig. 2a** and b show the pure anatase phases (JCPDS 21-1272), which are free of any discernible impurities and have prominent peaks at about 25° and 48°.

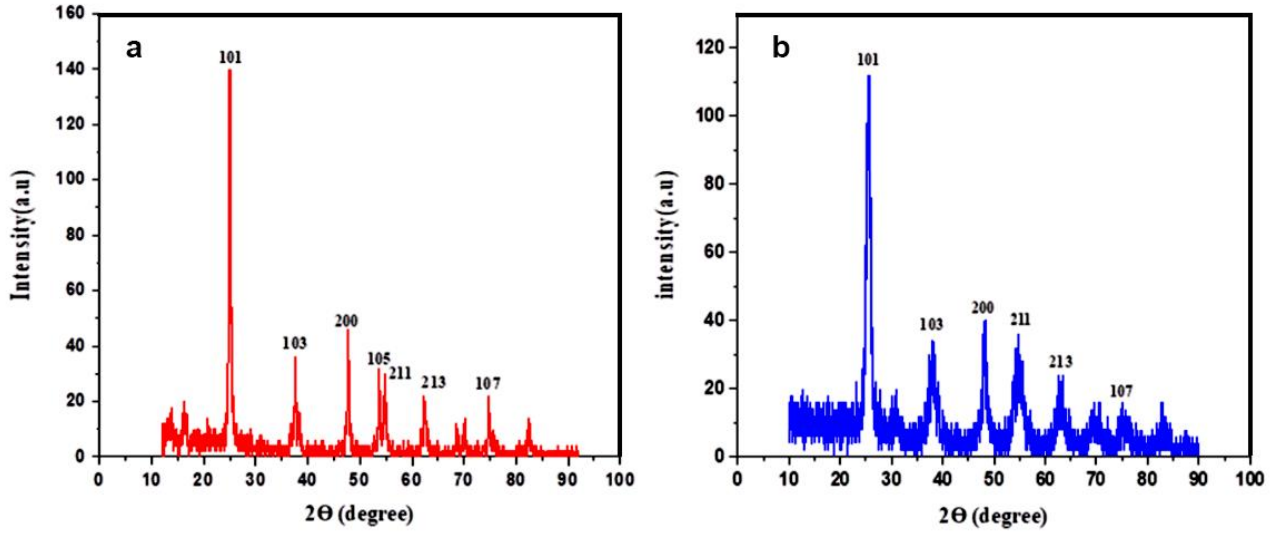

Figure 2: XRD patterns of TiO_2 nanoparticle synthesized by a) hydrothermal method b) sol-gel method.

Using the Scherrer formula, the average crystallite size (D) was determined. [16]:

$$D = k\lambda / \beta \cos\theta \text{ (nm)} \quad (2)$$

Where θ is the diffractive angle, β is the Full Width Half Maximum (FWHM), k is 0.94, and λ is 1.54060Å. Regarding samples S1 and S2. the estimated crystallite sizes were found to be 12 nm and 29 nm, respectively.

Compared to the sol-gel method, the hydrothermal process's higher temperature and pressure can encourage the growth of larger crystals, producing larger crystal sizes [17]. Additionally, the S2 sample's observed diffraction peaks showed a somewhat wider range, suggesting a smaller crystallite size than the sample. Additionally, we measured the lattice strain in the S1 and S2 specimens using the Williamson-Hall method. Plotting of βCosθ against 4Sinθ yields a straight line; the slope and intercept of this plot, which is obtained from the relationship, could be utilized to calculate the crystal's size and the strain ε . Crystal defects, crystallite size, and distortion of strain-induced peak widening were all determined using Williamson-Hall (W-H) plots Eq. (3) [18]:

$$\boldsymbol{\beta_{hkl} = \beta_D + \beta_\varepsilon} \quad \textbf{(3)}$$

$$\boldsymbol{\beta_{hkl} = \left(\frac{k\lambda}{Dcos\theta}\right) + 4\varepsilon tan\theta} \quad \textbf{(4)}$$

Rearrangement of Eq. 4 and 5 yields [19]:

$$\boldsymbol{\beta_{hkl}\, cos\theta = \left(\frac{k\lambda}{D}\right) + 4\varepsilon sin\theta} \quad \textbf{(5)}$$

where D is the dimension of the produced particle crystallites, λ is the wavelength of radiation (λ = 0.154051 nm), θ is the Bragg angle, θ is the shape factor, β is the lattice strain, β_{hkl} is the whole broadening of a peak, and β is the complete width at half maximum of the peak [20]. The outcome of this approach is shown in **Table 1** and **Fig. 3**. Compared to the Debye-Scherrer equation, the W–H methodology typically yields a smaller crystallite size because each approach makes different assumptions and considerations. As can be seen from the table, the fact that every diagram has a negative slope suggests that compressive strain is present in both the S1 and S2 samples.

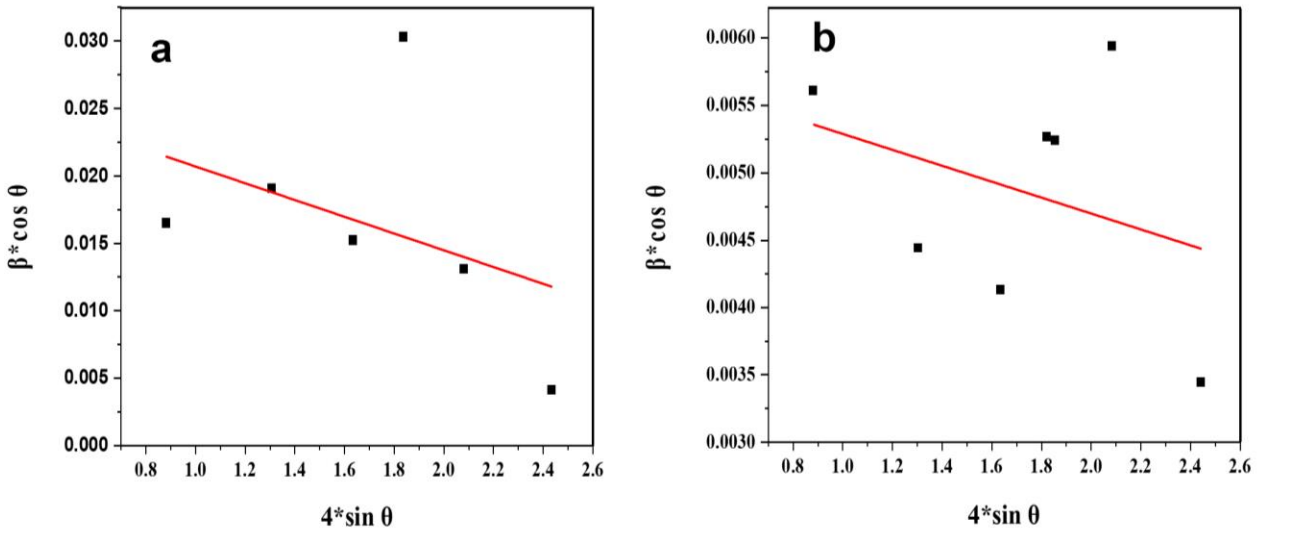

Figure 3: Williamson–Hall (W-H) plot of TiO_2 nanoparticle a) hydrothermal method b) sol-gel method.

Table 1: Lattice microstrain of TiO_2 NPs and crystallite size.

TiO_2 samples	Size of crystal (Scherrer equation) (nm)	Size of crystal (W–H equation) (nm)	Microstrain (ε)
TiO_2 (hydrothermal)	29.3127	25.1750	-0.00058
TiO_2 (sol-gel)	12.1940	5.5109	-0.00617

3.2 Morphological Properties

Morphological characterization of TiO_2 nanoparticles prepared by hydrothermal and sol-gel techniques was

conducted using field emission scanning electron microscope (FE-SEM), as displayed in **Fig. 4**. Due mostly to the primary aggregation of nanocrystalline TiO_2, the sol-gel sample findings demonstrate that several nanoparticles exhibit homogeneous shape with spherical form in various caves. The particle size is around 45.2 nm. However, the specimens subjected to hydrothermal treatment exhibit a remarkably uniform distribution of particles compared to the sol-gel samples, accompanied by a reduction in particle size (43.7 nm). It is noted that the particles demonstrate a distinct spherical morphology.

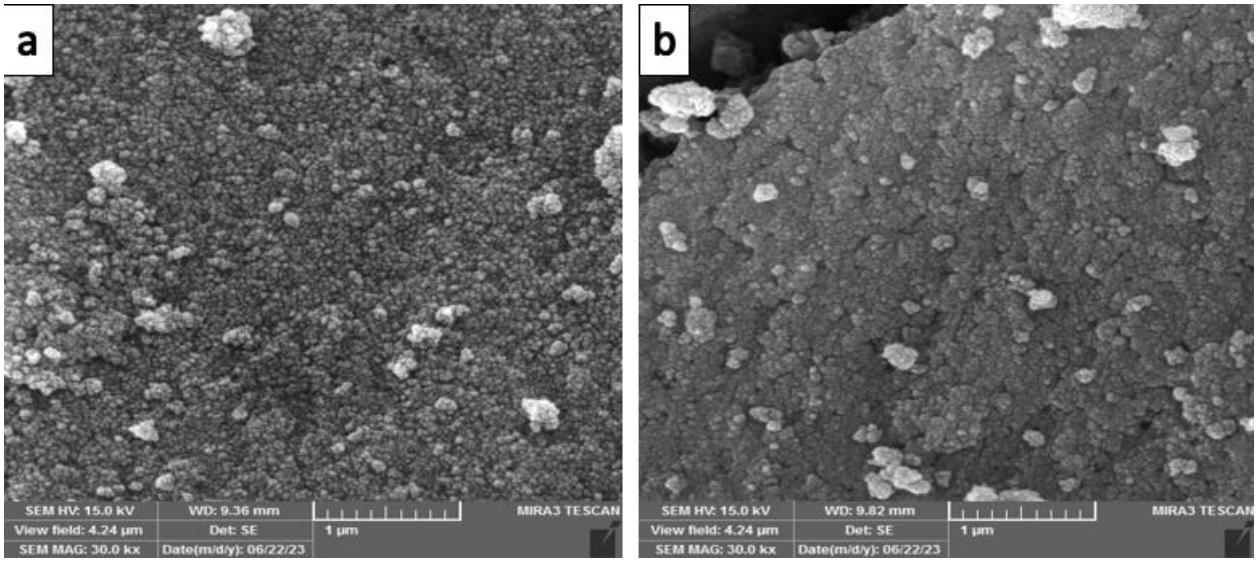

Figure 4: SEM images of TiO_2 nanoparticle a) hydrothermal method b) sol-gel method.

The surface area of the synthesized photocatalyst frameworks significantly impacts their effectiveness in environmental applications. A larger surface area provides more active sites for photocatalytic reactions, enhancing the interaction between the catalyst and pollutants, which leads to improved degradation rates. [21]. The porous structure provides better surface area, and this applies to the sample prepared by the hydrothermal method. It should be mentioned that SEM-produced powders have larger sizes of particles than XRD-produced ones. This is because SEM enables us to acquire sizes of particles that may consist of two or more grains of crystallite, while XRD offers the crystallite diameter. [22].

3.3 Zeta Potential Analysis

To determine the zeta potential of the TiO_2 nanoparticles, a qualitative analysis of homogeneity and the stability of titanium dioxide was conducted. The zeta potentials of the nanoparticles were determined to be -22.38 mV for the S1 nanostructure and -44.79 mV for the S2 nanostructure (See **Fig. 5)**. The zeta potential linked to the charge of surface properties of the TiO_2 nanostructure explains the ranges of stability of the scattered particles in the suspension. When the absolute value of the zeta potential exceeds 20 mV, the suspension is electrostatically stabilized. The general zeta potential criteria for enhanced stability are further confirmed negatively by the prepared suspension study. [23].

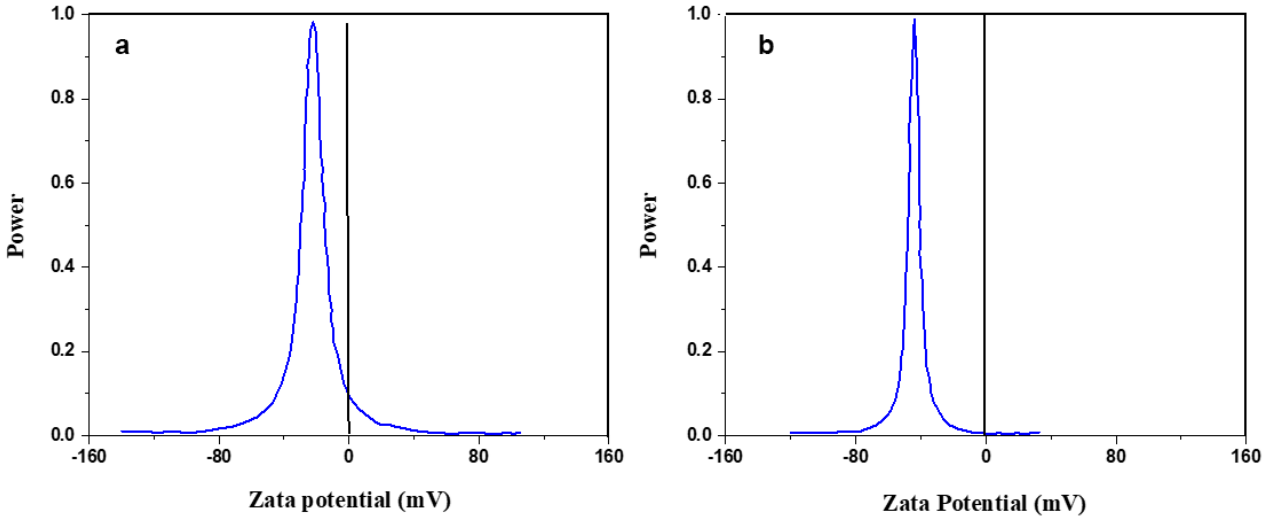

Figure 5: Zeta potential diagrams of TiO_2 nanoparticle a) hydrothermal method b) sol-gel method.

3.4 Optical and Spectroscopic Properties

Understanding the optical properties of materials is aided by the UV-vis analysis. The optical absorbance of TiO_2 nanostructures in the wavelength range of 200–1100 nm is shown in **Fig. 6**. The TiO_2 NPs exhibited strong UV absorption, and it was simple to identify the TiO_2 absorption edge. In the 200–390 nm range, TiO_2 showed a strong absorption. The S2 sample exhibited a noticeable blue shift toward shorter wavelengths. As shown in the **Fig. 6b**, the linear section of the spectral data was extended to α = 0 of a plot of $(\alpha h\nu)^2$ vs $(h\nu)$ to use the Tauc formula to establish the sample's direct bandgap energies.

$$(\mathbf{ahv})^{1/n} = \mathbf{A}(\mathbf{hv} - \mathbf{E_g}) \quad \textbf{(6)}$$

where A is a proportional constant, v is the vibration frequency, h is Planck's constant, $h\nu$ Is the photon energy, and α Is the absorption coefficient; Eg denotes the bandgap energy, whereas the kind of transition is indicated by n [24]. Depending on the type of transition, n can take on different values: n = 1/2 for a direct allowed transition, and n = 2 for an indirect allowed transition. **Table 2** displays the wavelength of the absorption edge and the band-gap values for S1 and S2, indicating that the E_g value for the sol-gel sample is less than those corresponding to the hydrothermal sample. The decrease in bandgap may be due to changes in the size of crystallite, morphology, and quantum confinement, which will all impact the bandgap [25].

Table 2: TiO_2 NPs' bandgap values and absorption edge wavelength.

TiO_2 samples	Bandgap energy (eV)	Absorption edge wavelength (nm)
TiO_2 (hydrothermal)	3.2	385
TiO_2 (sol-gel)	3	365

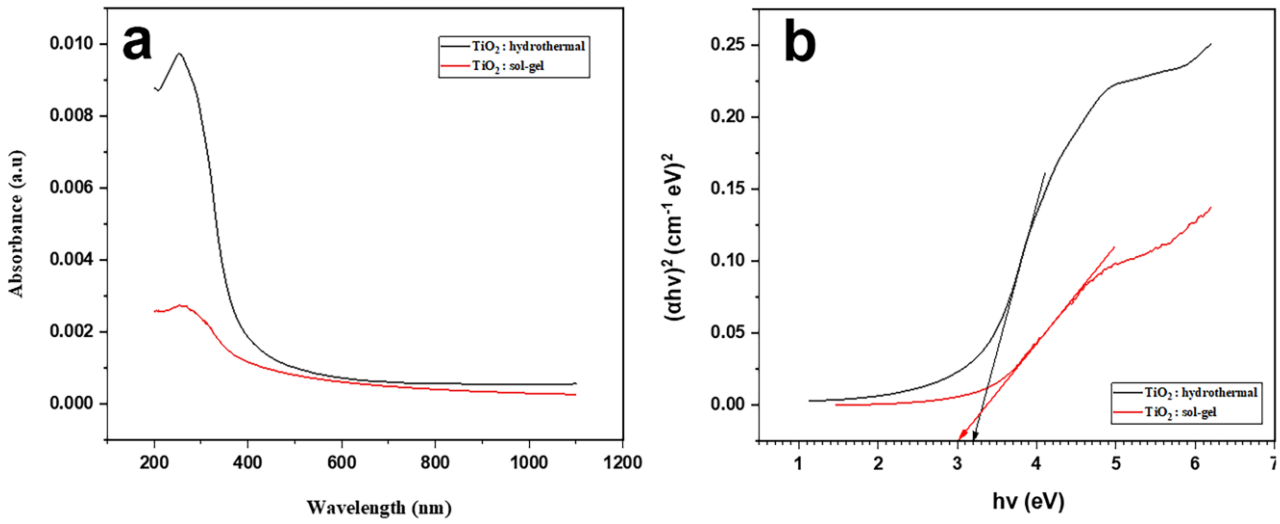

Figure 6: The UV–vis absorption spectra of TiO_2 nanoparticles. Variation of $(\alpha h\upsilon)^2$ vs. $(h\upsilon)$ for S1 and S2 is shown in an inset figure.

FT-IR spectroscopy was utilized to examine chemical bonds of the TiO_2 nanostructures prepared by hydrothermal and sol-gel methods in the range (400–4000 cm^{-1}), as displayed in **Table 3**. The presence of hydroxyl groups on the surface and molecules of water adsorbed in the interlayer region is shown by the peaks at 3410, 3381, and 4000 cm^{-1}. The peak at 2922 cm^{-1} is caused by the alkane group's C-H stretching vibrations. The alkane groups are provided by Titanium tetra isopropoxide (TTIP), which is used in the synthesis process. The peaks at 1635 and 1624 cm^{-1} were caused by the stretching vibrations of OH groups. Peaks that fall between 2500 and 2300 cm-1 indicate that the O=C=O bonds stretch. Additionally, the broad absorption band extending from 500 to 1000 cm^{-1} demonstrates the Ti-O-Ti bonds in the TiO_2 molecules' vibrational absorption. The 400–900 cm^{-1} infrared band represents the Ti–O stretching vibrations.

Table 3: FT-IR peaks of TiO_2 nanoparticles.

Chemical bond	Bond's location	
	TiO_2 (hydrothermal)	**TiO_2 (sol-gel)**
O-H hydroxyl groups	3410	3381
C-H stretching vibrations	2922	-
OH stretching vibrations	1635	1624
O=C=O bonds stretch	2360	2358
Ti–O stretching vibrations	449	451

3.5 Decay of Organic Contaminants in Industrial Wastewater by Photocatalysis

The sample's photocatalytic efficiency is determined by measuring the decay in the experiment for a specified catalyst load and duration. **Fig. 7** displays and compares the results of examining how S1 and S2 catalysts affect the number of organic pollutants removed from industrial wastewater when exposed to UV lamps. It can be claimed that TiO_2 (S1) had better degradation capabilities than TiO_2 (S2) because it had more empty sites. Consequently, when the levels of superoxide and hydroxyl radicals rise, it also increases the rate of degradation. The reduction in COD levels demonstrated the photocatalytic breakdown of oil and grease contaminants along with other organic pollutants in the industrial water. The photocatalytic process may produce intermediates and products that are more hazardous than the initial chemical. Therefore, the complete mineralization of CO_2 and water is the main goal of the treatment procedure. Thirty minutes after the light irradiation, the TOC content was measured to examine the degree of mineralization of industrial wastewater through the process of photocatalytic decomposition. **Fig. 7a** illustrates how the S1 and S2 effects cause the rate of mineralization to decrease. The effectiveness of S1 and S2 nanostructures photo-catalytically treating industrial wastewater is demonstrated in **Fig. 7b**, which also shows how well they remove oil and grease while reducing the levels of COD and TOC. As seen in **Fig. 7**, the S1 catalyst exhibits higher levels of photocatalytic activity than the S2 nano-powder catalysts. This can be caused by several things, such as surface form, increased specific surface area, crystal structure, and enhanced light sensitivity. [4]. The performance of synthesized photocatalysts in photocatalytic reactions is determined by their acid and basic sites. These locations affect catalytic activity, reactive species production, and reactant adsorption. [1].

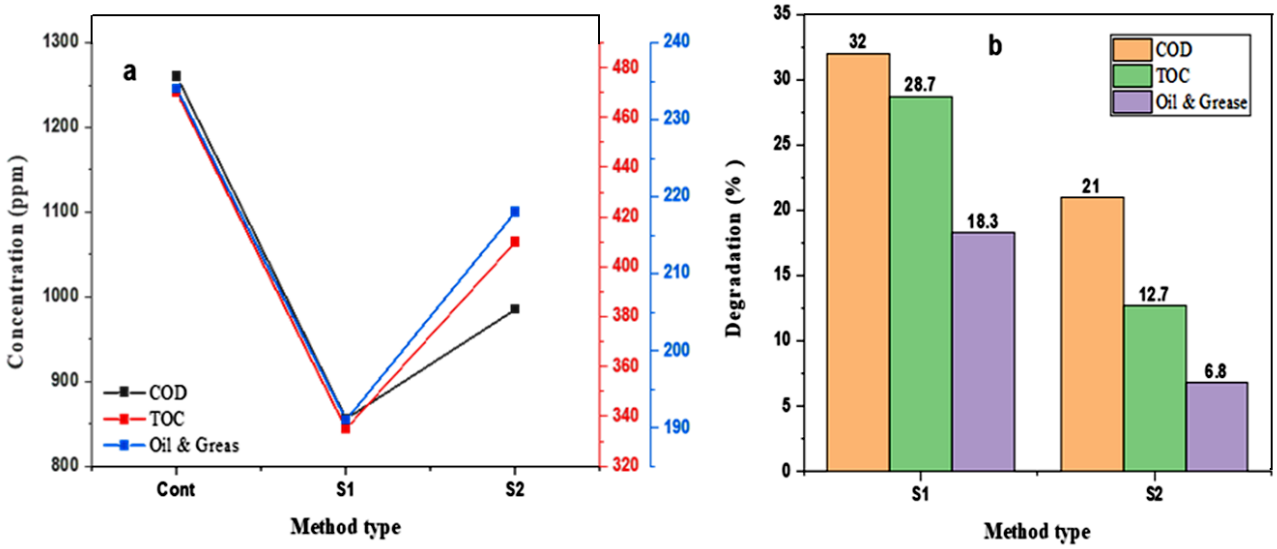

Figure 7: a) The concentration of organic pollutants removed by TiO_2 nano-powder in industrial wastewater when exposed to UV light. b) Photocatalytic degradation efficiency of S1 and S2 samples.

Polycyclic Aromatic Hydrocarbons (PAHs) in industrial wastewater can be identified by gas chromatography. Benzene rings combine to produce organic molecules known as polycyclic aromatic hydrocarbons (PAHs), which can be organized in a variety of ways and serve a variety of chemical and radical purposes. [26]. **Table 4** shows the concentration of 16 PAHs removed from industrial wastewater by S1 and S2 catalysts in comparison to the concentration before removal (control). **Table 4** shows that many organic compounds are under the detection limit (UDL), meaning that catalysts have eliminated them. Additionally, the photocatalytic degradation values of the TiO_2 (S1) catalyst are higher than those of the TiO_2 (S2) catalysts. The photodegradation of water pollutants for numerous other authors is shown in **Table 5**.

Table 4 The concentration of 16 PAHs removed by TiO_2 catalysts from industrial wastewater compared to the concentration before removal (control).

Compound identified	PAH level (ppm) removal using a photocatalyst supported by a UV lamp		
	Control (without catalyst)	TiO_2 (hydrothermal)	TiO_2 (sol-gel)
Acenaphthene	110	29	33
Acenaphthylene	201.4	57	60.4
Anthracene	98.5	32.6	35.5
Benzo (A) Anthracene	95	15.9	33.7
Benzo(B) Fluoranthene	102.6	23.9	40.3
Benzo (K) Fluoranthene	UDL	UDL	UDL
Benzo (G, H) Perylene	UDL	UDL	UDL
Benzo (A) Pyrenen	30.5	2.9	4.08
Chrysene	UDL	UDL	UDL
Dibenzo (A, H) Anthracene	UDL	UDL	UDL
Fluranthene	33	9.9	10.2
Fluroene	90.6	6.9	11.2
Indeno	UDL	UDL	UDL
Naphthalene	25	7.5	9.5
Phenanthrene	UDL	UDL	UDL
Pyrene	UDL	UDL	UDL

Table 5: The photodegradation of pollutants in water for this study and previous research

Authors	**Pollutants type**	**Catalyst**	**degradation efficiency**	**Duration**
Zhifeng Guo *et al* [27]	Phenol	TiO_2	76%	12h
Mushtaq, Kanza, *et al* [28]	ofloxacin	TiO_2	64%	3h
Khalilova *et.al* [29]	COD	TiO_2	40%	120 min
present work	Organic pollutants in petroleum refinery wastewater	TiO_2/S1	32%	30 min
		TiO_2/S2	21%	30 min

4. Conclusions

In this paper, TiO_2 NPs have been synthesized and characterized using sol-gel and hydrothermal techniques. The process of structural growth and morphology has been clarified, and many factors have been systematically investigated using techniques including XRD, FE-SEM, FT-IR, zeta potential, and UV-vis analysis. X-ray diffraction (XRD) analyses revealed that the TiO_2 has a pure anatase phase; the calculated crystallite size of the S1 and S2 samples was determined to be 29 nm and 12 nm, respectively. FE-SEM analysis was used to examine the particle size and surface area. The spherical shape of the nanoparticles was confirmed by FE-SEM measurements. According to the UV-Vis spectra, the Eg value for the sol-gel sample is lower than that of the hydrothermal sample. This method of TiO_2 photodegradation under UV light irradiation turned out to be a cost-effective and efficient way to rid water samples of both organic and inorganic contaminants. TiO_2 (S1) shows a higher photocatalytic degradation activity of wastewater pollutants than TiO_2 (S2) when exposed to UV light.

Acknowledgment

We would like to thank the University of Technology and the College of Applied Sciences in Baghdad, Iraq, for conducting this study.

Conflict of Interest

The authors declare that they have no conflict of interest.

References

[1] W. A. Muslim, T. M. Albayati, and S. K. Al-Nasri, "Decontamination of actual radioactive wastewater containing 137Cs using bentonite as a natural adsorbent: equilibrium, kinetics, and thermodynamic studies," *Sci. Rep.*, vol. 12, no. 1, p. 13837, 2022.

[2] S. Wang, C. Yu, X. Chen, K. Zhang, H. Gao, X. Yu, *et al.*, "Synthesis and characterization of $BaTiO_3/TiO_2$ heterojunction photocatalyst for novel application in photocatalytic degradation of TBBPA under simulated sunlight irradiation," *ChemistrySelect*, vol. 7, no. 45, p. e202202764, 2022.

[3] K. H. Aboud, S. M. H. AL-Jawad, and N. J. Imran, "Synthesis and characterization of flakes-like and flowers-like Ni: CdS nano films via hydrothermal technique for photocatalytic activity," *J. Mater. Sci. Mater. Electron.*, vol. 34, no. 11, p. 933, 2023.

[4] S. M. H. AL-Jawad, N. J. Imran, and K. H. Aboud, "Synthesis and characterization of Mn: CdS nanoflower thin films prepared by hydrothermal method for photocatalytic activity," *J. Sol-Gel Sci. Technol.*, vol. 100, pp. 423–439, 2021.

[5] X. Pan, S. Tang, X. Chen, H. Liu, C. Yu, Q. Z. Gao, *et al.*, "Temperature-controlled synthesis of TiO_2 photocatalyst with different crystalline phases and its photocatalytic activity in the degradation of different mixed dyes," *Russ. J. Phys. Chem. A*, vol. 96, no. Suppl 1, pp. S210–S218, 2022.

[6] S. M. H. Al-Jawad, O. N. Salman, and N. A. Yousif, "Influence of growth time on structural, optical and electrical properties of TiO_2 nanorod arrays deposited by hydrothermal method," *Surf. Rev. Lett.*, vol. 26, no. 03, p. 1850155, 2019.

[7] S. M. H. Al-Jawad, O. N. Salman, and N. A. Yousif, "Influence of titanium tetrachloride concentration and multiple growth cycles of TiO_2 nanorod on photoanode performance in dye sensitized solar cell," *Photonics Nanostructures-Fundamentals Appl.*, vol. 31, pp. 81–88, 2018.

[8] S. M. H. Al-Jawad, M. M. Ismail, and S. F. Ghazi, "Characteristics of diluted magnetic semiconductor based on Mn-doped TiO_2 nanorod array films," *J. Solid State Electrochem.*, vol. 25, no. 2, pp. 435–443, 2021.

[9] B. Guan, J. Yu, S. Guo, S. Yu, and S. Han, "Porous nickel doped titanium dioxide nanoparticles with improved visible light photocatalytic activity," *Nanoscale Adv.*, vol. 2, no. 3, pp. 1352–1357, 2020.

[10] W. He, Z. Fang, K. Zhang, X. Li, D. Ji, X. Jiang, *et al.*, "Continuous synthesis of a co-doped TiO_2 photocatalyst and its enhanced visible light catalytic activity using a photocatalysis microreactor," *RSC Adv.*, vol. 5, no. 68, pp. 54853–54860, 2015.

[11] S. M. H. Al-Jawad and M. M. Ismail, "Characterization of Mn, cu, and (Mn, cu) co-doped ZnS nanoparticles," *J. Opt. Technol.*, vol. 84, no. 7, pp. 495–499, 2017.

[12] J. Li, Q. Wu, and J. Wu, "Synthesis of nanoparticles via solvothermal and hydrothermal methods. 12," 2016, *Springer international publishing Switzerland*.

[13] R. S. Dubey, "Temperature-dependent phase transformation of TiO_2 nanoparticles synthesized by sol-gel method," *Mater. Lett.*, vol. 215, pp. 312–317, 2018.

[14] S. A. Talal *et al.*, "Effect of single doping and dual doping with Mn and Fe on the photocatalytic activity of TiO2 nanoparticles," *J. Sol-Gel Sci. Technol.*, vol. 2025, pp. 1-16, 2025.

[15] H. P. Shivaraju, N. Muzakkira, and B. Shahmoradi, "Photocatalytic treatment of oil and grease spills in wastewater using coated N-doped TiO_2 polyscales under sunlight as an alternative driving energy," *Int. J. Environ. Sci. Technol.*, vol. 13, pp. 2293–2302, 2016.

[16] L. Saikia, D. Bhuyan, M. Saikia, B. Malakar, D. K. Dutta, and P. Sengupta, "Photocatalytic performance of ZnO nanomaterials for self sensitized degradation of malachite green dye under solar light," *Appl. Catal. A Gen.*, vol. 490, pp. 42–49, 2015.

[17] A. Timoumi, W. Zayoud, A. Sharma, M. Kraini, N. Bouguila, A. Hakamy, *et al.*, "Impact of thermal annealing inducing oxidation process on the crystalline powder of In_2S_3," *J. Mater. Sci. Mater. Electron.*, vol. 31, pp. 13636–13645, 2020.

[18] O. N. Hussein, S. M. H. AL-Jawad, and N. J. Imran, "Efficient antibacterial activity enhancement in Fe/Mn co-doped CuS nanoflowers and nanosponges," *Bull. Mater. Sci.*, vol. 46, no. 3, p. 139, 2023.

[19] S. J. Singh, Y. Y. Lim, J. J. L. Hmar, and P. Chinnamuthu, "Temperature dependency on Ce-doped CuO nanoparticles: a comparative study via XRD line broadening analysis," *Appl. Phys. A*, vol. 128, no. 3, p. 188, 2022.

[20] S. M. H. Al-Jawad, A. A. Taha, A. M. Redha, and N. J. Imran, "Influence of nickel doping concentration

on the characteristics of nanostructure CuS prepared by hydrothermal method for antibacterial activity," *Surf. Rev. Lett.*, vol. 28, no. 01, p. 2050031, 2021.

[21] G. Singh, M. K. Ubhi, K. Jeet, C. Singla, and M. Kaur, "A review on impacting parameters for photocatalytic degradation of organic effluents by ferrites and their nanocomposites," *Processes*, vol. 11, no. 6, p. 1727, 2023.

[22] H. Khojasteh, M. Salavati-Niasari, and S. Mortazavi-Derazkola, "Synthesis, characterization and photocatalytic properties of nickel-doped TiO_2 and nickel titanate nanoparticles," *J. Mater. Sci. Mater. Electron.*, vol. 27, pp. 3599–3607, 2016.

[23] A. A. Taha, S. M. H. AL-Jawad, and L. F. A. AL-Barram, "Improvement of cancer therapy by TAT peptide conjugated gold nanoparticles," *J. Clust. Sci.*, vol. 30, no. 2, pp. 403–414, 2019.

[24] P. Singla, O. P. Pandey, and K. Singh, "Study of photocatalytic degradation of environmentally harmful phthalate esters using Ni-doped TiO_2 nanoparticles," *Int. J. Environ. Sci. Technol.*, vol. 13, pp. 849–856, 2016.

[25] F. G. Hone and F. B. Dejene, "Cationic concentration and pH effect on the structural, morphological and optical band gap of chemically synthesized lead sulfide thin films," *J. Mater. Res. Technol.*, vol. 8, no. 1, pp. 467–474, 2019.

[26] F. C. Monteiro, I. D. L. Guimaraes, P. de Almeida Rodrigues, J. V. da A. de Pinho, and C. A. Conte-Junior, "Degradation of PAHs using TiO_2 as a semiconductor in the heterogeneous photocatalysis process: A systematic review," *J. Photochem. Photobiol. A Chem.*, vol. 437, p. 114497, 2023.

[27] Z. Guo, R. Ma, and G. Li, "Degradation of phenol by nanomaterial TiO_2 in wastewater," *Chem. Eng. J.*, vol. 119, no. 1, pp. 55–59, 2006.

[28] K. Mushtaq, M. Saeed, W. Gul, M. Munir, A. Firdous, T. Yousaf, *et al.*, "Synthesis and characterization of TiO_2 via sol-gel method for efficient photocatalytic degradation of antibiotic ofloxacin," *Inorg. Nano-Metal Chem.*, vol. 50, no. 7, pp. 580–586, 2020.

[29] H. K. Khalilova, S. A. Hasanova, and F. G. Aliyev, "Photocatalytic removal of organic pollutants from industrial wastewater using TiO_2 catalyst," *J. Environ. Prot. (Irvine,. Calif).*, vol. 9, no. 06, p. 691, 2018.